small methods
www.small-methods.com

Tailoring the Morphology of a Diketopyrrolopyrrole-based Polymer as Films or Wires for High-Performance OFETs using Solution Shearing

*Preetam Dacha, Mike Hambsch, Darius Pohl, Katherina Haase, Markus Löffler, Tianshu Lan, Xinliang Feng, Bernd Rellinghaus, and Stefan C. B. Mannsfeld**

Conjugated polymers often show efficient charge carrier transport along their backbone which is a primary factor in the electrical behavior of Organic Field Effect Transistor (OFETs) devices fabricated from these materials. Herein, a solution shearing procedure is reported to fabricate micro/nano wires from a diketopyrrolopyrrole (DPP)-based polymer. Millimeter to nanometer long polymer wires orientated in the coating direction are developed after a thorough analysis of the deposition conditions. It shows several morphological regimes—film, transition, and wires and experimentally derive a phase diagram for the parameters coating speed and surface energy of the substrate. The as-fabricated wires are isolated, which is confirmed by optical, atomic force, and scanning electron microscopy. Beside the macroscopic alignment of wires, cross-polarized optical microscopy images show strong birefringence suggesting a high degree of molecular orientation. This is further substantiated by polarized UV-Vis-NIR spectroscopy, selected area electron diffraction transmission electron microscopy, and grazing-incidence wide-angle X-ray scattering. Finally, an enhanced electrical performance of single wire OFETs is observed with a 15-fold increase in effective charge carrier mobility to 1.57 $cm^2 V^{-1} s^{-1}$ over devices using films (0.1 $cm^2 V^{-1} s^{-1}$) with similar values for on/off current ratio and threshold voltage.

1. Introduction

Solution shearing, a form of meniscus-guided coating, is known for high-throughput and low-cost fabrication of thin films.[1] It is a powerful tool to achieve excellent molecular arrangement, stacking, and uniformity in the films with minimal material waste.[2–4] The final morphology of a material deposited by solution shearing is influenced by various factors such as surface energy of the substrate, solution concentration and viscosity, speed, and substrate temperature. All these factors define whether there is any deposition of the material at all or whether a film forms, in which case we found them to be comprised of pure or mixed phases of 2D islands and wires.[2,5] Understanding the interplay between these factors can help to control the deposition process and achieve desired morphologies of a specific material.

The formation of films and wires using meniscus-guided coating has been a

P. Dacha, M. Hambsch, K. Haase, T. Lan, X. Feng, S. C. B. Mannsfeld
Center for Advancing Electronics Dresden (cfaed)
Technische Universität Dresden
01069 Dresden, Germany
E-mail: stefan.mannsfeld@tu-dresden.de

P. Dacha, K. Haase, S. C. B. Mannsfeld
Faculty of Electrical and Computer Engineering
Technische Universität Dresden
01069 Dresden, Germany

D. Pohl, M. Löffler, B. Rellinghaus
Dresden Center for Nanoanalysis (DCN)
Center for Advancing Electronics Dresden (cfaed)
Technische Universität Dresden
01069 Dresden, Germany

T. Lan, X. Feng
Faculty of Chemistry and Food Chemistry
Technische Universität Dresden
01069 Dresden, Germany

T. Lan, X. Feng
Max Planck Institute of Microstructure Physics
Weinberg 2, 06120 Halle (Saale), Germany

The ORCID identification number(s) for the author(s) of this article can be found under https://doi.org/10.1002/smtd.202300842

DOI: 10.1002/smtd.202300842

topic of discussion for a variety of materials. In 2010, Farcau et al. reported on a meniscus instability causing parallel and perpendicular arrays of centimeter-long gold colloid nanoparticles under specific coating conditions.[6] Stick and slip behavior resulted in parallel wire-like formations, while perpendicular alignment was attributed to critical density triggered particle pinning. Qu et al. furthered this discussion with similar observations for conjugated polymers (CPs)[5] where a higher charge carrier mobility in the wires formed along the shearing direction was obtained compared to a film deposited under the same conditions. Further, the role of surface-free energy in governing the meniscus instabilities and understanding its relation with the coating speed was discussed. Rocha et al., addressed this issue with the use of piezo shearing to reduce these instabilities and achieve a continuous film.[2] However, a complete understanding of the coating behavior of CPs in relation to surface free energy and coating speed to discuss the meniscus instabilities for film, film-to-wire transition, and wire formation is yet to be explored.

Additionally, several attempts were made to produce aligned, wire-like assemblies of CPs using nano grooves[7] and PDMS stamping[8,9] techniques resulting in better charge transport properties of the fabricated organic field effect transistors (OFETs). Kim et al., discussed the formation of CP-based nanowires, but the use of drop casting resulted in randomly distributed wires.[10] Further, work on large area CP arrays using coaxial focused electro-hydrodynamic jet (CFEJ) printing resulted in highly ordered structures with location-specific placement.[11,12] Though there have been several reports that process CP films and wires using self-assembly and nanoconfinement methods,[5,6,9,13–16] the ease of fabrication and the size range of the wires is still a challenge due to the utility of PDMS stamping, transfer techniques or utilization of nanogrooved blades resulting in a complicated processing setup. However, the interplay between surface energy, coating speed, and the resulting morphology of films and wires produced through solution shearing remains unexplored. Delving into this relationship and proficiently controlling morphology via solution shearing could potentially enhance the exploitation of enhanced charge transport characteristics in OFETs.

In this work, we are investigating the relation between the surface energy, coating speed, and the resulting morphology for the donor-acceptor CP, poly[2,5-(2-octyldodecyl)−3,6-diketopyrrolopyrrole-alt-5,5-(2,5-di(thien-2-yl)thieno [3,2-b]thiophene)] (DPP-DTT) which has been reported for its excellent charge transport properties and relatively high degree of crystallinity.[3,10,12,17,18] When coated on substrates with different surface energies, it was observed that films, wires, and a mixed morphology region can be obtained depending on the speed of the solution shearing process. Noticeably, better packing and order resulted in a fifteen-fold increase in charge carrier mobility of the OFETs measured on single wires compared to the films sheared on substrates of the same surface energy. To demonstrate the correlation between surface energy, coating speed, and morphology we employ a variety of self-assembled monolayers (SAMs) with trimethoxysilane (TMS) and different alkyl chain lengths on Si/SiO_2 substrates. With increase in solution shearing speed on these TMS-coated samples, a clear shift in morphology from films to wires along with a mixed morphology region was observed. This work opens avenues to explore wires for sensing and opto-electronic applications.[19,20]

2. Results and Discussion

2.1. Substrate Surface Modification

Figure 1a shows a simplified drawing for the solution shearing process. The surface energy of the substrate which plays a key role in controlling the morphology of the material, was modified in this research by the use of different SAMs of alkyl silanes. The importance of SAMs in organic semiconductor (OSC) devices has been discussed in the literature in the past with a focus on OFETs where they showed potential for improved order and packing in OSC films resulting in better charge transport.[3,21–23] In this study, we examine how the combination of surface energy modified through the use of different SAMs on SiO_2 substrates and coating speed affects the morphology of shear-coated DPP-DTT. For that we employed different trimethoxy silanes with different alkyl chain lengths, namely butyl(B), octyl(O), decyl(D), dodecyl (DD), hexadecyl (HD), and octadecyl (OD). TMS was selected as anchor group due to its lower reactivity compared for example to trichlorosilanes and therefore a better control over the preparation of the SAMs.[24] All the SAMs were coated under the same conditions as reported previously,[25] the structures of all SAMs used in this research are depicted in Figure S1, Supporting Information. Contact angle measurements were performed on various SAM-coated substrates using water, dichlorobenzene (DCB), and DPP-DTT in DCB (3 mg ml^{-1}) solutions as shown in Figure 1c and tabulated in Table S1, Supporting Information. The measurements reveal a clear shift in the water contact angle with increasing length of the alkyl chains.[3,22,25] Additionally, a significant shift in contact angle by 20° was observed from DTMS to DDTMS, which also resulted in a decrease in surface energy by almost 10 mN m^{-1} as can be seen in Figure 1d. It is important to note that in this particular region of surface energy we observe a stark shift in both film morphology and corresponding absorption spectra which will be discussed later in this paper.

2.2. Characterization of Morphological Properties using POM, AFM, and SEM

It is clear from Figure 1 that the increase in the SAM's alkyl side chain length impacts the surface energy of the substrate and thereby the water contact angle.[23] Furthermore, the morphology of the OSC film is affected by the speed of coating, leading to a change in their charge transport properties.[3] In this paper, we discuss the impact of changes to the surface energy and coating speed on the morphology of DPP-DTT thin films. As expected, we find that the greater the substrate water contact angle, i.e., the lower the surface energy of the substrate, the lower the chance to obtain continuous (electrically connected) films that could work as an active device layer.

Polarized optical microscopy (POM) images as presented in Figure S2, Supporting Information, reveal the morphological changes observed in DPP-DTT with a change in surface energy while keeping the speed constant at 500 μm s^{-1}. When sheared

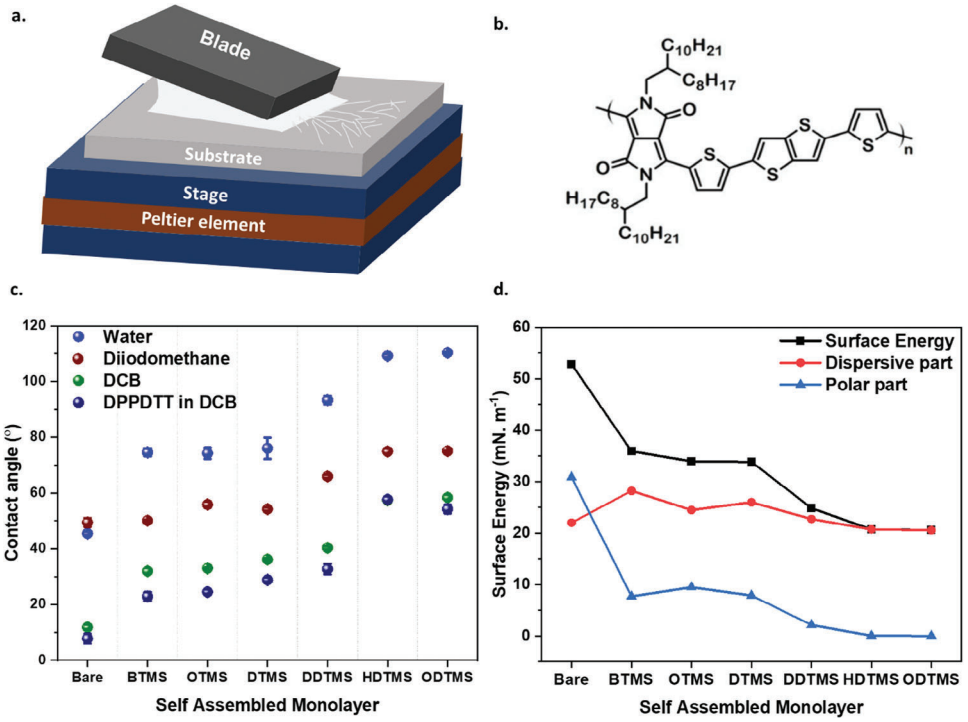

Figure 1. a) Schematic of the device fabrication using solution shearing technique. b) Chemical structure of DPP-DTT and c) The as-measured contact angles with water, diiodomethane, dichlorobenzene, and DPP-DTT in dichlorobenzene (3 mg ml^{-1}) solutions on the respective SAMs and d) surface energy obtained on different SAMs using the *Owens, Wendt, Rabel, and Kaelble* method.[26]

on ODTMS, which has the lowest total surface energy of 20.58 mN m^{-1}, the OSC tends to form wires, as opposed to films observed on substrates with higher surface energies ranging from 33.85 to 52.86 mN m^{-1}. Interestingly, on DDTMS with a surface energy of 24.86 mN m^{-1}, a mixed morphology of films and wires is observed. Although this phenomenon has been extensively studied and reported,[5] a clear distinction between films and wires has not been discussed thus far. From the POM images it is evident that, when the surface energy reached a value below 21 mN m^{-1}, distinct wires that were isolated from each other were observed. These wires show clear birefringence, pointing to a high degree of order among the polymer chains within the wires and a possibility of liquid crystalline or semi-crystalline arrangement of the polymer.[27] Moreover, to test whether these wires are indeed completely isolated without any amount of OSC thin film between them, bright and dark field optical microscopy images were taken as shown in Figure S3, Supporting Information, where the wires are observed to be entirely isolated. Although, the optical microscopy analysis alone does not represent conclusive evidence for the above claim, the atomic force microscopy (AFM) results as shown in **Figure 2**a–f fully support the interpretation that there is no film between the individual wires.

The AFM images clearly show that when DPP-DTT is shear coated on different SAMs of varying surface energy values under the same conditions, a transition from a film to wires occurs. The images in Figure 2a–d are in good agreement with the consistent fibrillar pattern seen in DPP-DTT films with the introduction of mixed morphological pattern at a surface energy of 24.86 mN m^{-1}. This observation is consistent with the existing literature on surface energy and morphological understanding.[5,28–30] Further, the AFM images from samples with the surface energy value less than 21 mN m^{-1}, which correspond to the HDTMS and ODTMS SAMs, confirms the absence of a thin film between the wires as seen in Figure S4, Supporting Information. Furthermore, from RMS roughness measurements as shown in Figure S5, Supporting Information, we see that the transition from high to low surface energy resulted in an increased surface roughness.

Scanning electron microscopy (SEM) was also used to resolve the micro- and nanometer-scale morphology of the wires obtained on ODTMS substrates and to probe their chemical composition. The SEM images in **Figure 3**a–d show the range of wires that can be produced in terms of their length and width. Here, the length of the wires corresponds to the long axis region while the width to its side-to-side extension. Apart from the extensive range of micro wires on the substrate as seen in Figure S3, Supporting Information, a statistical analysis on several nanometer-level SEM images confirms that the length of nanowires falls within the range of 250 – 1000 nm. The width was typically in the range of 40 – 100 nm based on the dataset as shown in Figure S6, Supporting Information. Elemental analysis performed on a micrometer-sized wire as shown in Figure 3e,f corroborates the finding of isolated wires with the Si and O elements predominantly traced on the substrate and C, N, and S series observed on the wire. The elemental graph has been shown in Figure S7, Supporting Information. Overall, POM, AFM, and SEM studies confirm that DPP-DTT coatings on substrates with varying surface energy values at the same speed can yield films, mixed morphology regions, and wires. Additionally, shearing on

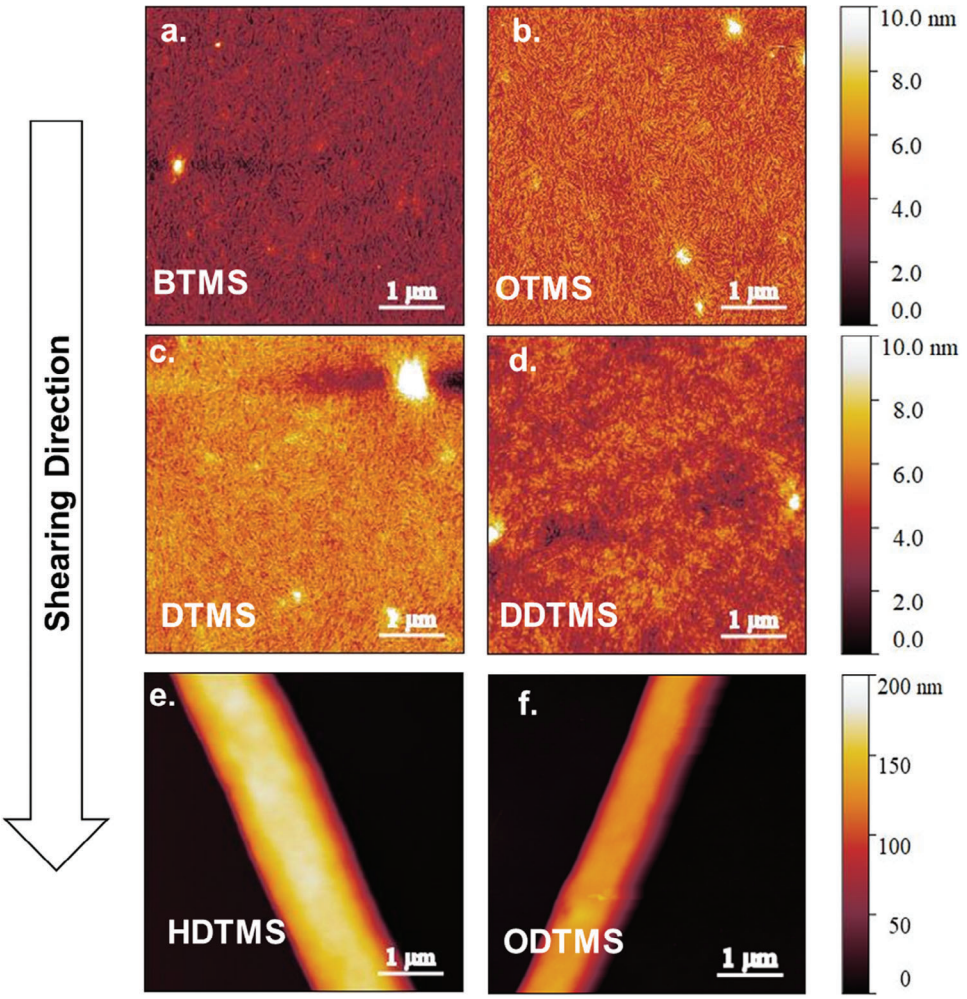

Figure 2. AFM a–f) images showing the morphological changes of DPP-DTT coated on BTMS, OTMS, DTMS, DDTMS, HDTMS, and ODTMS SAMs at 500 μm s^{-1}.

low surface energy substrates, such as ODTMS, can result in the formation of isolated wires in the shearing direction of the sample which showed clear birefringence under POM, as observed in **Figure 4**a. To determine the angular alignment of the wires in respect to the shearing direction, DPP-DTT solutions with concentrations of 3, 6, and 9 mg ml^{-1} were shear coated onto ODTMS substrates with 500 μm s^{-1}. The distribution of the angles in respect to the shearing direction for the different solution concentrations is shown in Figure 4b. The angular orientation of the polymer wires is found to be in the similar range on either side of the coating direction, irrespective of the solution concentration, although further studies are required to identify ways to control this.

So far, morphological changes have been observed when DPP-DTT was shear coated at a constant speed on different substrates with varying surface energy values and solution concentration. It is noteworthy that the solution concentration appears to have little effect on the angular spread of wires, as shown in Figure 4b. Hence, we restricted the further analysis to the lowest concentration of the solution, 3 mg ml^{-1}. The relation between surface free energy, coating speed, and morphology of the OSC was further investigated by performing additional experiments at various coating speeds. The results of these experiments were used to assemble the phase diagram shown in **Figure 5**, which illustrates the four different morphological regimes observed when solution shearing: films, mixed morphology, wires, and no material deposition (none). These findings provide valuable insights into the effect of coating speed and surface energy on the morphology of the OSC, and can aid in the optimization of OSC fabrication for various applications.

It can be seen that when DPP-DTT was sheared at speeds ranging from 50 μm s^{-1} to 3000 μm s^{-1}, on high surface energy samples, uniform films were formed. The color map in Figure 5 represents the morphological changes from film, mixed morphology, wires, and no film. Studies on surface energy models have proposed a wire-like deposition region at higher speeds and lower surface energy, which is compatible with the morphological transitions in our study as shown in Figure 5.[5] However, any further increase in the coating speed on low surface energy substrates results in no deposition of the CP.

We also wanted to investigate whether these morphological changes translate into observable differences in the

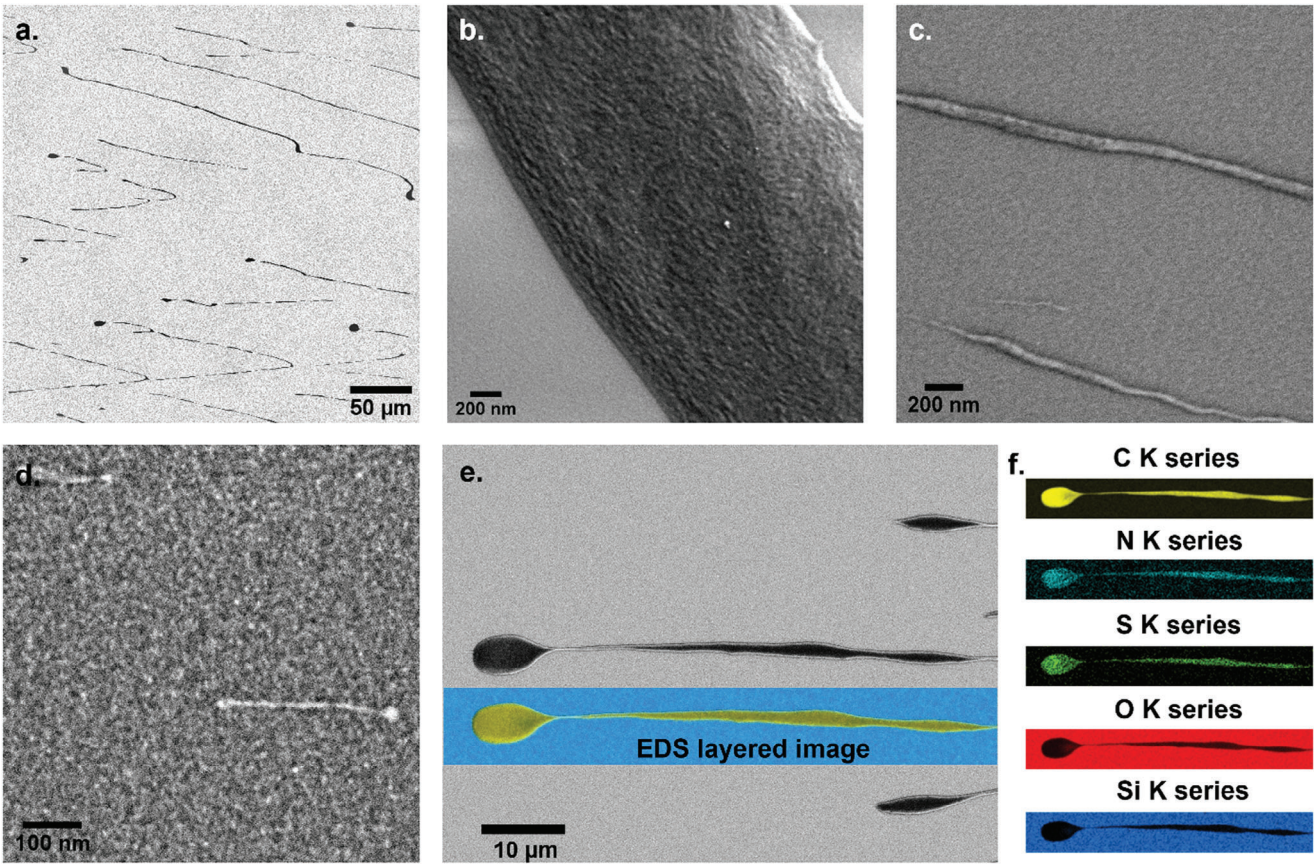

Figure 3. Scanning electron microscopy images of DPP-DTT wires on ODTMS showing a), micro, b) and c), sub micro, d) nanometer level wires which are completely isolated from each other. e) Elemental analysis and the layered image of a micro wire and f) presence of elements C, N, and S in the wire while depicting Si and O on the remaining area. The elemental analysis map can be seen in Figure S7, Supporting Information.

corresponding optical absorption spectra from the deposited material, and to assess any optical anisotropy associated with the wires. For this, we performed spectral analysis using UV-Vis-NIR spectroscopy, preparing both samples with film or wire on it with the lowest possible surface energy value of 20.58 mN m^{-1} using ODTMS.

Figure 6a shows the polarized UV-Vis-NIR spectrum of DPP-DTT coated on quartz/ODTMS substrates. In addition, the UV-Vis-NIR spectra of DPP-DTT is also shown in Supplementary Figure 8 for reference. As the absorbance values recorded from these measurements were very low, the data obtained for both film and wire samples have been normalized with respect to the maximum absorption peak of the respective measurements. It is commonly observed that DPP-DTT exhibits a dual-band absorption[18,27,31] and we clearly see an increased red shift in the absorption for the wires which can be attributed to the strong intermolecular coupling.[28,29,32] The two absorption peaks between 725 and 900 nm correspond to the π-π* transitions of 0–1 and 0-0, respectively.[13,31] A clear redshift of these peaks to a greater extent of 50 nm is evident as shown more clearly in Figure S9, Supporting Information.

We calculated the dichroic ratio of the film and wire absorption for the 0-0 and 0–1 peaks and the results are shown in Figure 6b. The absorption dichroic ratio (D) which is given by $A_{0°}/A_{90°}$, where A is the absorption intensity of the peak in consideration, can be used to understand the absorbance anisotropy when the polarization of the incident light is parallel and perpendicular to the shearing direction. The D value for the 0-0 peak changes from 0.8 to 1.5 while for the 0–1 peak it shifts from 1.1 to 0.9 for the film and wire, respectively which is in good agreement with the literature.[32] A D value of 1.5 for the 0-0 peak along with the red shift of the peak for the wire sample indicates a higher molecular order within the polymer which is consistent with literature.[33] Therefore, the polarized absorption spectra analysis corroborates that the birefringence observed in the wires under POM as evidenced in Figure 4 is due to a higher degree of polymer chain order than that of the film phase.

2.3. Grazing-Incidence Wide-Angle X-Ray Scattering (GIWAXS) Analysis

In the next step, we performed grazing-incidence wide-angle X-ray scattering (GIWAXS) measurements to investigate the structure in the wires and compare it to the structure of films prepared on the same SAM. In **Figure 7**a the 2D-GIWAXS image of a wire sample prepared on ODTMS with a speed of 500 µm s^{-1} is shown. The scattering intensity from the wire samples was very low compared to film samples due to the much lower scattering volume. To increase the signal intensity, we rotated the

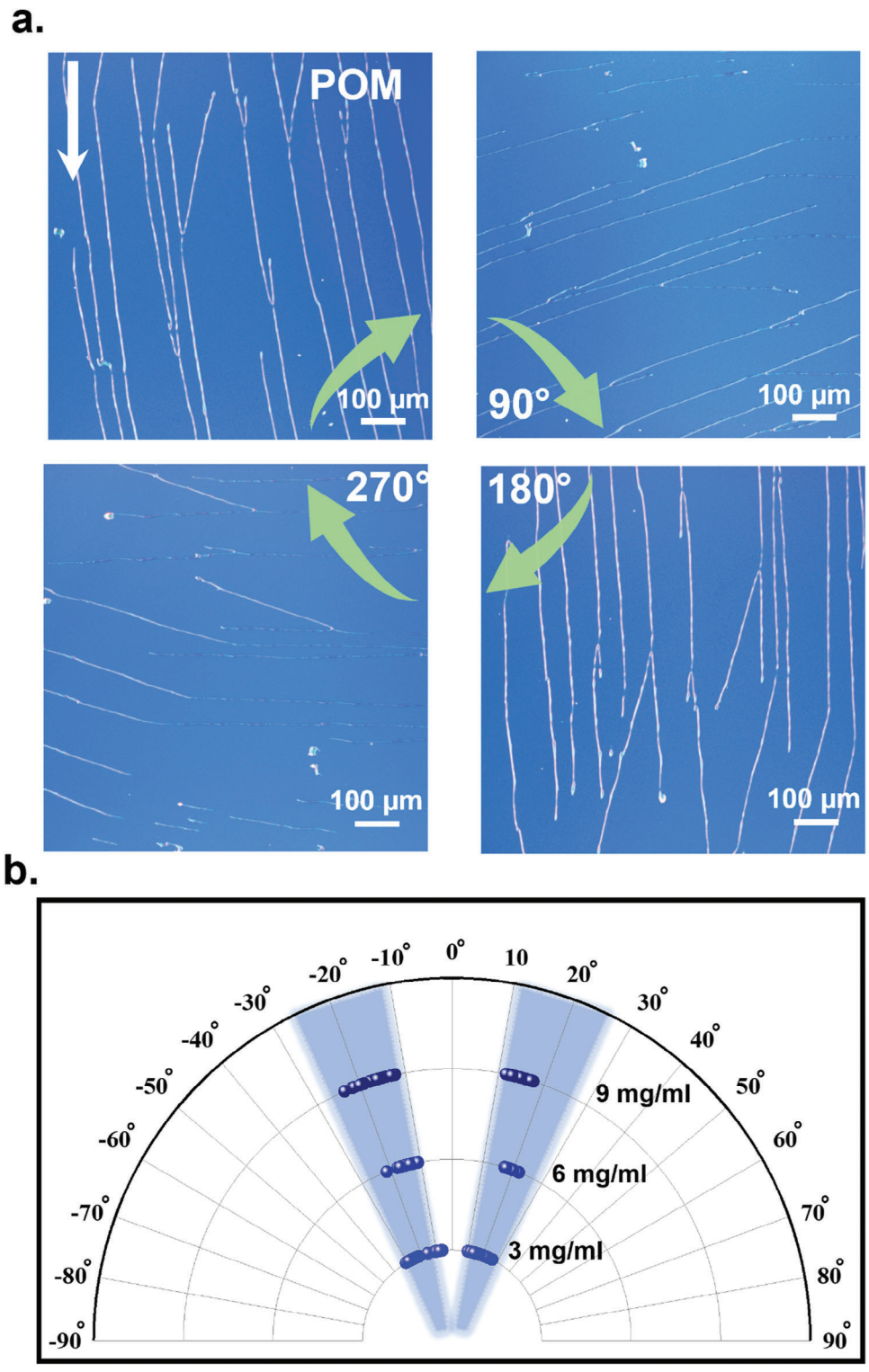

Figure 4. a) Cross polarized optical microscopy images of DPP-DTT wires rotated along the shearing direction to show birefringence. The wires were shear coated on ODTMS using 3 mg ml^{-1} solution at 500 µm s^{-1}. b) Polar plot showing the angular spread seen in wires for varied concentration of the solution. 0° here corresponds to the shearing direction.

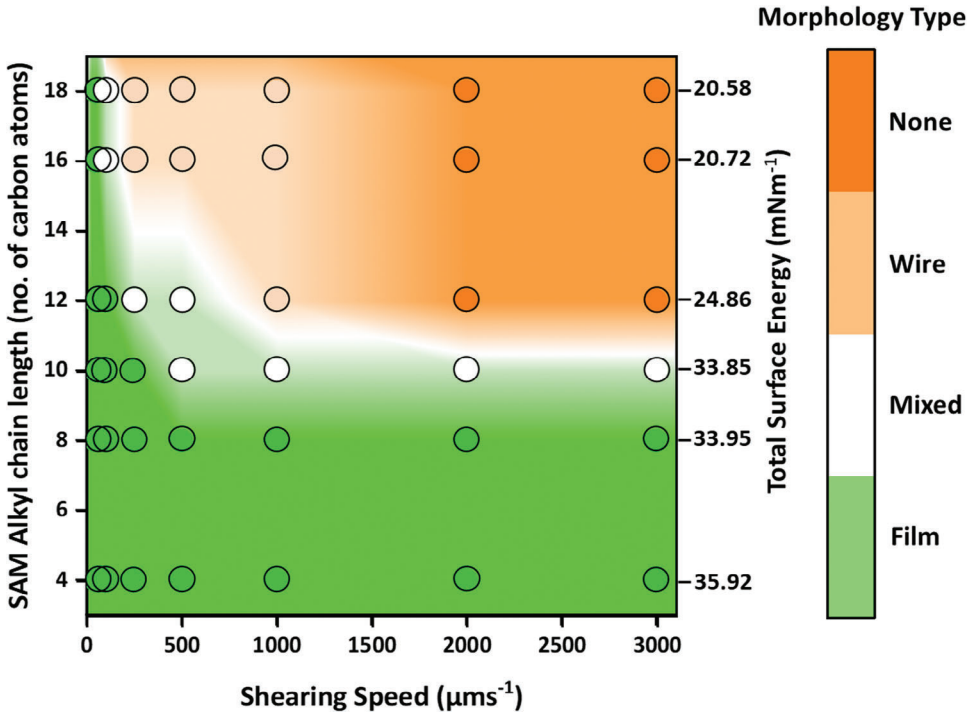

Figure 5. Phase diagram of DPP-DTT in DCB solution sheared on different SAMs representing the morphological changes observed at different coating speeds. The left y-axis here corresponds to the number of carbon atoms in the alkyl chain of the respective SAM and the right y-axis shows the total surface energy. The color bar depicts the different morphologies in the phase diagram observed for the DPP-DTT polymer. The circled points are the experimental parameters and values used for the majority of the experiments in this work; the background shows an interpolation to the experimental values.

sample 360° during exposure to integrate over all the wires on the substrate. In addition, we increased the signal-to-noise ratio by subtracting the background of a blank silicon wafer substrate. After these additional steps, we were able to identify three out-of-plane peaks and at least one in-plane peak. For a more detailed analysis of the peak positions, we plotted the out-of-plane (Figure 7c) and in-plane (Figure 7d) intensity profiles. The positions of the peaks and the corresponding distances are summarized in Table S2, Supporting Information. There we can assign the three out-of-plane peaks at $Q_z = 0.32$ Å^{-1}, 0.62 Å^{-1} and 0.93 Å^{-1} to the first three orders of the lamellar stacking, which corresponds to a stacking distance of around 20 Å. In addition, there is a very weak peak at around $Q_z = 1.7$ Å^{-1} corresponding to a spacing of 3.7 Å, which can be attributed to the π-π stacking. Both values the lamellar and the π-π distance fall very well in the reported ranges for thin films of this material.[27,34] Upon closer inspection of the in-plane profiles (Figure 7d) we were able to distinguish two peaks, the larger one at $Q_{xy} = 1.47$ Å^{-1} can

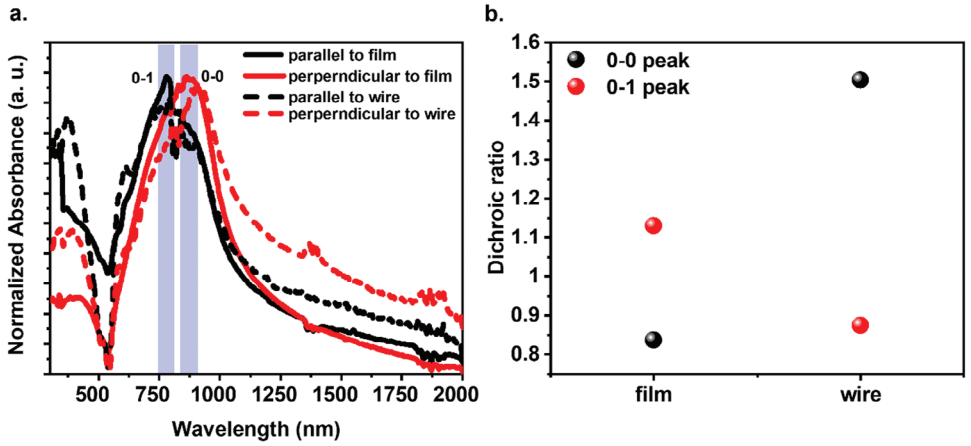

Figure 6. a) Polarized UV-Vis-NIR spectra of DPP-DTT wire and film samples on ODTMS depicting an absorption peak shift. b) Peak position shift in major peaks of absorption observed in DPP-DTT. Parallel and perpendicular here correspond to the spectral polarization to the shearing direction.

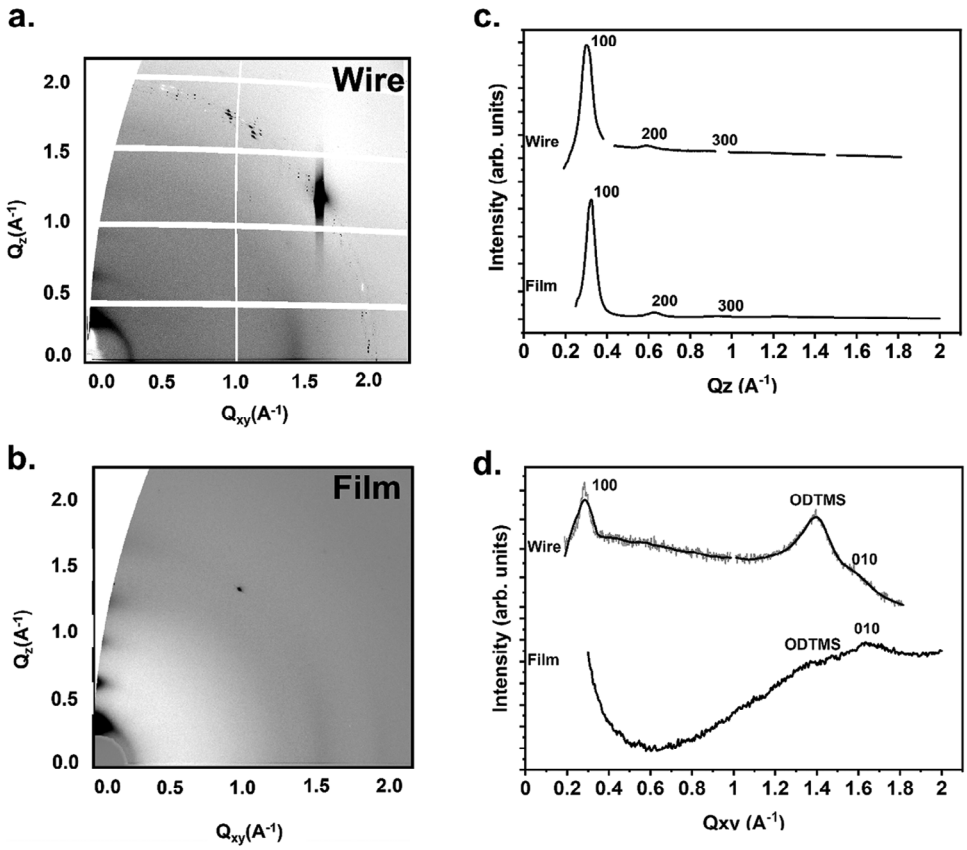

Figure 7. 2D GIWAXS images of a) a DPP-DTT wire and b) DPP-DTT film sample. c) Out-of-plane and d) in-plane intensity profiles for the wire and films sample on ODTMS.

be attributed to the ODTMS monolayer, which is in good agreement with the literature.[25] The reason that the peak is so pronounced is the large amount of area not covered by the DPP-DTT. The second smaller peak at Q_{xy} = 1.61 Å^{-1} can be attributed to the in-plane contribution of the π-π stacking and corresponds to a stacking distance of ≈3.9 Å. The presence of contributions of both the lamellar stacking and the π-π stacking peak in-plane and out-of-plane confirms the presence of both edge-on and face-on orientation existing in the wires.[32]

The 2D-GIWAXS image of a shear-coated film on ODTMS measured parallel to the coating direction is shown in Figure 7b. Similar to the wire case, we can identify multiple orders of out-of-plane peaks. The exact positions can be seen more clearly in the out-of-plane intensity profile in Figure 7c (Q_z = 0.32 Å^{-1}, 0.63 Å^{-1} and 0.93 Å^{-1}) and correspond to a lamellar stacking distance of ≈20 Å, which matches with the wire sample. In the in-plane intensity profile there are no peaks visible for the lamellar stacking but a peak at Q_{xy} = 1.65 Å^{-1} representing a π-π stacking distance of 3.81 Å^{-1}. The absence of the lamellar peaks and the presence of the π-π stacking peak in the in-plane profile and not out-of-plane profile indicate that a majority of the crystalline domains of the polymer orient edge-on in respect to the substrate. From a qualitative comparison between the wires and film it looks like the amount of edge-on oriented crystals in the film in comparison to the amount of face-on oriented domains is higher than in the wires. One possible explanation could be that in the film sample there is much more interface between the polymer and the ODTMS coated substrate resulting in an increase in the ratio of edge-on orientation since this is the preferential orientation of the polymer on ODTMS.[3,35] Therefore, the GIWAXS measurements revealed that the packing of the crystalline parts of the wires and the film is almost similar with only slight variations in the π-π stacking distance.

2.4. Transmission Electron Microscopy – Selected Area Electron Diffraction

To verify the GIWAXS results for single wires, selected area electron diffraction (SAED) using transmission electron microscopy (TEM) was performed. It was found, that the wires are extremely sensitive to the beam and only a low dose measurement using fast detectors could reveal the crystalline structure of single polymer wires. The SAED pattern in **Figure 8**a shows two pronounced reflections at 0.485 nm^{-1} (20.6 Å) and 2.56 nm^{-1} (3.9 Å) best seen in the intensity profiles as in Figure 8c. This spacing can be attributed to the low index diffraction spots (100) and (010) of the assumed structure. The (100) and (010) reflection are found to be perpendicular to the wire direction. Similar SAED results are achieved for the continuous film sample as shown in Figure 8b

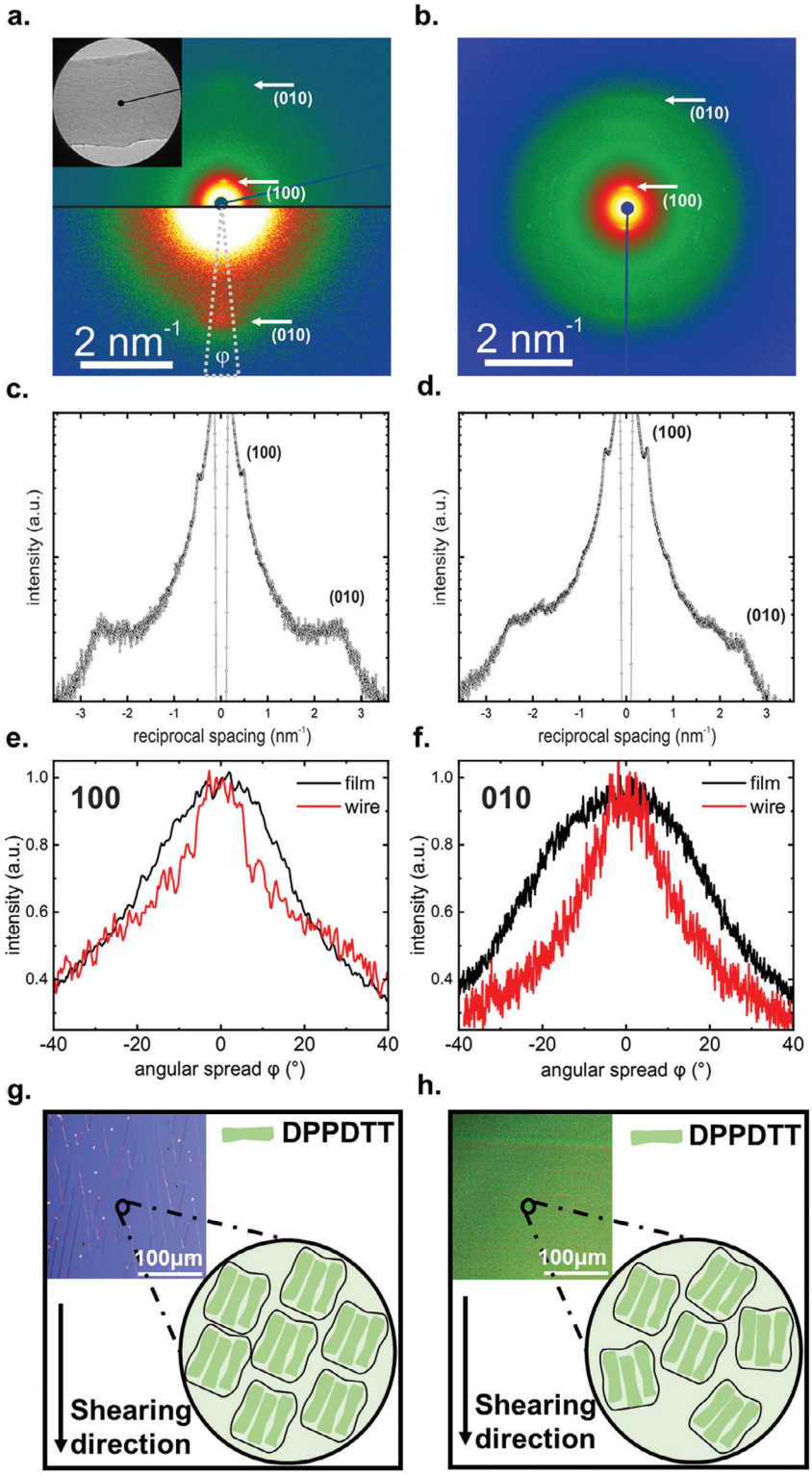

Figure 8. Selected area electron diffraction (SAED) of a) a single wire and b) a film of DPP-DTT. In order to highlight the less intense (010) reflection, the SAED pattern in (a) is shown with different contrast settings in the upper and lower halfves of the image. The inset shows selected region of the wire. c,d) Radial intensity profiles across the SAED patterns in (a) and (b) with marked (100) and (010) reflections corresponding to lattice spacings of 20.6 Å and 3.98 Å, respectively. e,f) represent tangential intensity profiles obtained from angular cross sections of the (010) and (100) reflections for both the wire (red) and the thin film (black). The area marked with a dashed line in the bottom half of (a) indicates corresponding angular broadening φ of the (010) reflection in the SAED pattern. g,h) indicate an exaggerated schematic of the texture width (i.e., the distribution of in-plane polymer orientations) in the wire (g) and in the film (h) as deduced from the SAED patterns. Insert show the POM images of the wire and film.

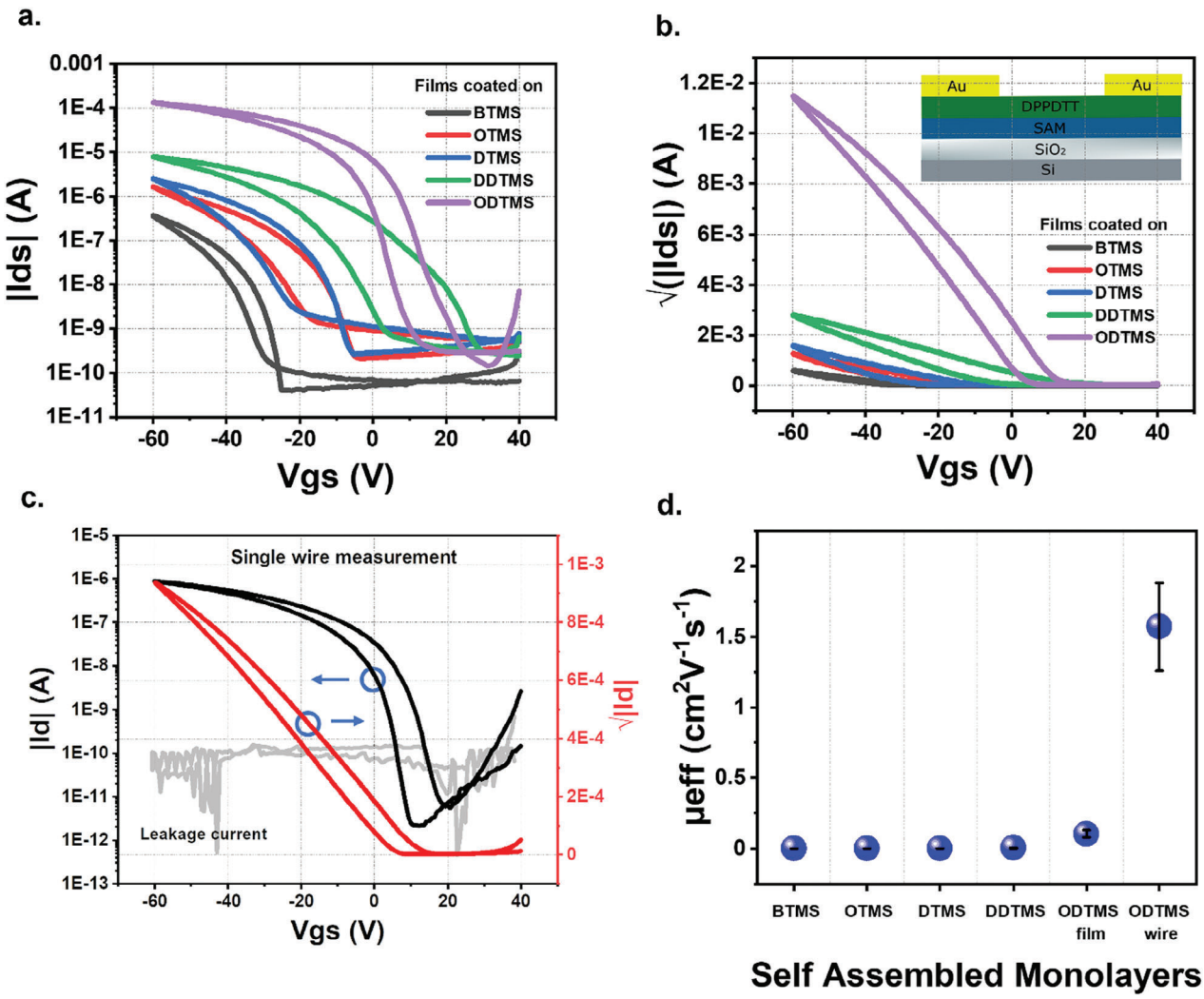

Figure 9. Transfer characteristics presented a) as semi-logarithmic plots and b) as square root plots for devices using the various SAMs along with the device architecture (inset). c) Transfer characteristics of an exemplary single wire device and d) the summary of the average effective mobility values of devices using films on the various SAMs in comparison to the single wire devices.

with the intensity profiles as in Figure 8d. Similar to the wire, a pronounced peak at 0.444 nm^{-1} (22.5 Å) and at 2.48 nm^{-1} (4.03 Å) is found corresponding to the (100) and (010) orientation.

The occurrence of the (100) and (010) in the same direction can be attributed to the presence of both edge-on and face-on molecule orientation in the wire which fits well with the GIWAXS data for the wires as shown in Figure 7. In order to determine if the wire exhibits greater molecular orientation than the film, angular cuts were made on both the (010) and (100) peaks, as depicted in Figure 8 (e) and (f) respectively. The results indicate that the diffraction spots in the wire are less broadened than those in the film, confirming a higher degree of alignment in the wires along their long axis which could be beneficial for charge transport along the wire.[20] From POM, UV-Vis, GIWAXS, and SAED analysis we conclude a more preferential molecular arrangement of the polymer chains in the wire compared to the film. A schematic visualization of the proposed arrangement of the crystalline regions of the polymer in the wires and the film are illustrated in Figure 8g,h.

2.5. Organic Field Effect Transistors (OFETs)

DPP-DTT as a thin film, has been well studied in OFETs in the past.[3,22] To investigate the effect of the higher degree of alignment in the wires fabricated in this study, we prepared single-wire OFETs. For comparison, film-based OFETs were fabricated that were solution sheared on different SAMs to correlate the effect of silanes (thereby effect of surface energy) to the wire-based OFETs as seen in **Figure 9**a. The bottom-gate top-contact (BGTC) architecture was employed with 50 nm thick, thermally evaporated Au top contacts that define devices with 200 µm channel length and 4500 µm channel width as shown in the inset of Figure 9b.

Figure 9a,b show the $|I_{DS}|$ and $\sqrt{|I_{DS}|}$ versus gate voltage (V_{GS}) characteristics respectively of the DPP-DTT films on different SAMs measured at a drain voltage (V_{DS}) of -60 V and the performance metrics of the devices are summarized in **Table 1**. Herein, the devices were measured along the shearing direction. We observe that with the decrease in surface energy of the substrate achieved by the SAMs with increasing alkyl chain lengths, the

Table 1. Extracted electrical parameters of the OFETs.

SAM	Shearing temperature [°C]	Threshold Voltage, V_{TH}[V]	Maximum mobility, μ_{max} [$cm^2\ V^{-1}\ s^{-1}$]	Average mobility, μ_{av} [$cm^2\ V^{-1}\ s^{-1}$]	Effective mobility, μ_{eff} [$cm^2\ V^{-1}\ s^{-1}$] [a)]	I_{ON}/I_{OFF}
BTMS films	100	−31.70 ± 2.56	$6.5 * 10^{-4} \pm 1 * 10^{-4}$	$6.4 * 10^{-4} \pm 1.6 * 10^{-4}$	$1.87 * 10^{-4} \pm 4.4 * 10^{-5}$	3×10^3
OTMS films	100	−18.97 ± 1.93	$2 * 10^{-3} \pm 1 * 10^{-3}$	$1.8 * 10^{-3} \pm 9.6 * 10^{-4}$	$1.5 * 10^{-3} \pm 8.9 * 10^{-4}$	7×10^3
DTMS films	100	−15.36 ± 1.35	$2 * 10^{-3} \pm 8 * 10^{-4}$	$1 * 10^{-3} \pm 9.2 * 10^{-4}$	$8 * 10^{-4} \pm 1 * 10^{-4}$	7×10^3
DDTMS films	100	24.83 ± 0.81	$5 * 10^{-3} \pm 3 * 10^{-3}$	$4.5 * 10^{-3} \pm 2 * 10^{-3}$	$4 * 10^{-3} \pm 2 * 10^{-3}$	2×10^4
ODTMS wire	100	14.45 ± 8.71	2.45 ± 1.69	1.61 ± 0.22	1.57 [b)] ± 0.31	5×10^5
ODTMS films	130	11.55 ± 7.62	0.16 ± 0.063	0.116 ± 0.02	0.104 ± 0.02	3×10^5

[a)] calculated based on [36]; [b)] average of 10 single wire devices.

on- and off current have increased gradually while the threshold voltage (V_{TH}) strongly shifted towards more positive voltages. To avoid the over-estimation of charge carrier mobilities of the devices, care has been taken to calculate the effective charge carrier mobility (μ_{eff}) values apart from the maximum mobility (μ_{max}) and average mobility (μ_{av}). The μ_{eff} values ensure that the most transparent mobility values are reported.[36] Films prepared by using increased shearing temperature on the ODTMS SAM (Figure S10, Supporting Information) clearly outperformed the films on all other SAMs with a μ_{eff} of 0.1 $cm^2\ V^{-1}\ s^{-1}$. The mobility versus the V_{GS} plot comparing the films and the wires is shown in Figure S11, Supporting Information.

Figure 9c represents the $|I_{DS}|$ and $\sqrt{|I_{DS}|}$ versus V_{GS} characteristics measured at a V_{DS} of -60 V for a single-wire OFET device. From this data, it is evident that the single wire devices measured are on par with the films on ODTMS in terms of V_{TH} which is 14 ± 8 V in comparison to the 12 ± 8 V for the films. A similar trend was observed for the on- and off ratio of the single wire and film devices which is for both in the range of 10^5. Interestingly, for the charge carrier mobility we observe a significant increase with a μ_{eff} value of 1.57 ± 0.3 $cm^2\ V^{-1}\ s^{-1}$ for wires which is fifteen times higher than the μ_{eff} value of the films on ODTMS SAM (0.1 ± 0.02 $cm^2\ V^{-1}\ s^{-1}$). This increase in mobility can be attributed to the more preferential alignment of the polymer in the wire as has been discussed in the SAED section. The μ_{eff} value of the single-wire device as mentioned in Table 1 has been reported after careful consideration of an average of 10 single wire devices. Further, their comparison with literature is shown in Table S3, Supporting Information, confirming the OFETs to be at par with reported values. The μ_{eff} values for different SAM-based OFETs along with single-wire device data are shown in Figure 9d. While the best reported maximum mobility value for DPP-DTT was 4.8 $cm^2\ V^{-1}\ s^{-1}$ as shown in Table S3 and Figure S12, Supporting Information, this value reduces to 0.48 $cm^2\ V^{-1}\ s^{-1}$ when calculated for the effective mobility value according to the literature.[18,36] Therefore, the significant fifteen-fold increase in μ_{eff} for single wires compared to the films is, to the best of our knowledge, the highest reported μ_{eff} value for this material. This opens the avenue for high performing transistor array fabrication by solution shearing.

3. Conclusion

To summarize, we employed solution shearing to fabricate wires that are oriented along the shearing direction using the semiconducting polymer, DPP-DTT. We derived a phase diagram that visualizes the morphological transitions from films to a mixed morphology, wires, and eventually the complete absence of material deposition. A wide range of wires were fabricated with varying lengths and widths and characterized using OM, AFM, and SEM. Findings from POM, GIWAXS, SAED TEM, and polarized UV-Vis-NIR spectroscopy indicate a preferential molecular alignment in the wires over that of films. Finally, single-wire OFETs outperformed the devices based on DPP-DTT films demonstrating a 15-fold improvement in μ_{eff}, resulting in a charge carrier mobility of 1.57 $cm^2\ V^{-1}\ s^{-1}$.

4. Experimental Section

Chemicals and methods: *Preparation of Solution*: Poly[2,5-(2-octyldodecyl)−3,6-diketopyrrolopyrrole-alt-5,5-(2,5-di(thien-2-yl) thieno[3,2-b] thiophene)] was purchased from Ossila Ltd. with an average molecular weight (M_w) of 203956 and PDI of 3.09 (M0311A2). BTMS was purchased from abcr Chemicals, OTMS, DTMS, HDTMS, and ODTMS from Sigma Aldrich, and DDTMS from Thermo Scientific. A 3 mg of DPP-DTT was stirred in 1 ml of o-DCB at 500 rpm and 100 °C under ambient conditions prior to film fabrication.

Transistor Fabrication: *Device Fabrication and Measurement*: Heavily doped silicon (Si) wafers with a thermally grown wet oxide of 300 nm were used as substrates for the devices. Prior to use, all the substrates went through a cleaning cycle for 15 min each of DI water, acetone and isopropanol in an ultrasonication bath in the same order. Post sonication, the substrates were dried using N_2.

Self-assembled monolayers were coated using the procedure described in literature.[25] A 3 mM solutions of various SAMs in Trichloroethylene (TCE- 99% pure from Sigma Aldrich) were prepared and the solution was spin-coated on the silicon substrates at 3000 rpm for 30 s. A 10 s spreading time was used between the deposition of solution on the substrate and the start of spin coating to encourage the complete coverage of the substrate with the solution. Afterwards, the sample was placed in a desiccator along with few milliliters of ammonium hydroxide solution (28%–30% water) in vacuum overnight. The samples were removed after around 12 hours and thoroughly ultrasonicated with toluene. Samples were rigorously cleaned further with toluene to ensure the removal of any residue of the silane.

For the OSC solution shearing, the blade angle was set at 8° with a gap of 20 µm between the edge of the blade and the substrate. The blade was also coated with ODTMS. 7 µL of polymer solution for a 3 cm × 1 cm Si/SiO_2/SAM substrate was injected at the interface between the substrate and the blade. During coating, for all SAMs, the substrate temperature was maintained at 100°C and speed was varied from 50 to 2000 µm s^{-1} as required to obtain the respective morphology. To compare the wires and films on ODTMS, it was necessary to coat films at a substrate temperature of 130°C and a speed of 500 µm s^{-1} to ensure that the comparison of OFETs has a constant coating speed for all films on different SAMs. After coating, the samples were transferred onto a hot plate set at the target temperature of 165°C for 10 minutes. Finally, Au source and drain electrodes with a thickness of 50 nm were deposited by thermal evaporation using shadow masks under high vacuum of 10^{-7} mbar with a deposition rate of 1.5 Å s^{-1}.

All devices were measured utilizing a Keysight B1500 Semiconductor Analyzer in a dark room. The field-effect mobility (μ_h) was calculated using the equation.

$$\mu_h = \frac{2L}{WC_i}\left(\frac{\partial\sqrt{|I_{DS}|}}{\partial V_{GS}}\right)^2 \quad (1)$$

Here, I_{DS} is the drain current, C_i is the capacitance per unit area of the dielectric, W is the channel width, L is the channel length, and V_{GS} is the gate voltage. The V_{TH} was obtained from the intercept of the linear fit of the $\sqrt{|I_{DS}|}$ versus V_{GS} curve and the x-axis. In this report, the C_i was 11.5 nF. cm^{-2} and was unchanged irrespective of the SAMs.[23] The channel width and length for all film OFETs were 4500 µm and 200 µm respectively. All single wire devices had a channel width of ≈1 µm and a varied channel length between 65 and 70 µm. The coating, annealing, morphology, and electrical measurements were performed in an ambient atmosphere with a relative humidity of about 30%.

Contact Angle Measurements: The contact angle measurements were performed with a Data Physics OCA series goniometer. The water and diiodomethane contact angle measurements were performed on the samples followed by using the Owens, Wendt, Rabel, and Kable (OWRK) method for the calculation of the surface energy.[26]

AFM and Optical Microscopy: Surface morphology and roughness of semiconductor film images were obtained with a Flex Axiom from a Nanosurf atomic force microscope using tapping mode and TAP-190Al-G non-conducting tips from Budget Sensors were used. Optical images were taken using a Zeiss Axio Imager.M2m microscope.

Polarized UV-Vis-NIR Spectroscopy: The Spectroscopy measurements were performed with a Cary 5000 UV-Vis-NIR spectrophotometer. 1×1 inch Quartz substrates purchased from Techinstro Ltd. were used for the measurements. The substrates were cleaned by ultrasonication in soap water, DI water, acetone and IPA each for 15 minutes before drying them using N_2. Self-assembled monolayers were coated using the same procedure as stated above.

Scanning Electron Microscopy: SEM was conducted using a Zeiss Gemini SEM 500 scanning electron microscope operated at electron energies between 3 keV and 0.4 keV.

EDS analysis was performed using an Oxford Max^N 150 mm^2 detector installed on the same system and using a primary electron energy of 3 keV.

SEM images of the wires were analyzed using the FIJI software. First, the "tubeness" filter[37] is applied with an appropriately selected sigma value. For images of the nanowires, a custom filter is applied to enhance the contrast of wires in the shearing direction. The resultant image is then subjected to a ridge-detection algorithm,[38,39] which is cleaned up manually to fix eventual overlaps. Finally, the resultant image is filtered for wires of a certain aspect ratio to avoid measuring non-wire shaped particles. Finally, since the wires are straight, the Feret's diameter is a good measure of wire length.

Transmission Electron Microscopy (TEM)– Selected Area Electron Diffraction (SAED): Transmission electron microscopy measurements have been conducted using a JEOL JEM F200 operated at 200 kV acceleration voltage equipped with a GATAN OneView CMOS camera for fast imaging. Since the polymer wires are extremely beam-sensitive, special care was taken to acquire unmodified diffraction data. First, illumination conditions have been set such that, the material do not alter during imaging due to radiolysis for at least 1 second. A time series, of a so-far not illuminated area, was taken and then analyzed. After 1.8 seconds (45 frames), the diffraction spots vanished, giving a critical dose of about 30 $e.nm^{-2}$. The shown SAED pattern is therefore the summation of the images before reaching the critical dose.

For SAED measurements, the TEM Cu-grid, coated with ODTMS served as the substrate for the films, which were applied through solution shearing. For the wire-based measurements, a thermal transfer technique was employed due to the inability to coat the wires directly on the Cu-grid. Initially, the wires were shear coated on the Si/SiO2/ODTMS substrate and then transferred onto a 100 nm carbon-coated Cu-grid. This transfer process involved stamping the wires onto a commercially available Nitto thermal release tape. Using a cantilever attached to a glass slide connected to a micromanipulator, the wires on the thermal release tape were precisely aligned with the target Cu-grid and brought into contact. The stack was subsequently baked at 110°C for 2–3 min to release the wires from the tape. Finally, the glass slide was gradually raised to gently detach the thermal release tape from the Cu-grid, resulting in the Cu-grid with wires, which was used for the SAED measurements.

Grazing-Incidence Wide-Angle X-Ray Scattering: Grazing-incidence wide-angle X-ray scattering (GIWAXS) measurements of the DPP-DTT wires were performed at XRD1 at ELETTRA, Trieste, Italy. The beam energy was 12.4 keV and the spot size of the beam was 200 µm x 200 µm. A Dectris Pilatus 2 M area detector was placed 400 mm behind the sample. The sample-detector distance and the beam center on the detector were verified using lanthanum hexaboride as a reference. The incidence angle of the beam was 0.12° and the sample was exposed for 180 s to the beam while being rotated 360°. The rotation was necessary to get sufficient scattering intensity due to the low scattering volume in the wire samples. In addition, a background subtraction using a blank silicon substrate to reduce the background scattering was performed.

The GIWAXS measurements of the DPP-DTT films were performed at BL11-NCD SWEET at ALBA, Spain. The beam energy was 12.4 keV and the spot size was 70 µm (vertical) x 150 µm (horizontal). A Rayonix LX255HS area detector was placed 167 mm behind the sample. The sample-detector distance and the beam center on the detector were verified using chromium(III) oxide as a reference. The incidence angle of the beam was 0.12° and the sample was exposed for 3 – 5 s to the beam. All the data were analyzed using WxDiff.

Supporting Information

Supporting Information is available from the Wiley Online Library or from the author.

Acknowledgements

The authors acknowledge Elettra Sincrotrone Trieste for providing access to its synchrotron radiation facilities and the authors thank Luisa Barba for assistance in using beamline XRD1. The research leading to this result has been supported by the project CALIPSOplus under Grant Agreement 730872 from the EU Framework Programme for Research and Innovation HORIZON 2020. Part of these experiments were performed at BL11 – NCD SWEET at ALBA Synchrotron with the collaboration of ALBA staff. The authors thank Marc Malfois for help in setting up the experiment. The authors acknowledge the use of the facilities in the Dresden Center for Nanoanalysis (DCN) at the Technische Universität Dresden. K. H. further acknowledges the financial support by the TU Dresden and the Professorinnenprogramm III des Bundes und der Länder.

Open access funding enabled and organized by Projekt DEAL.

Conflict of Interest

The authors declare no conflict of interest.

Author Contributions

P.D., M.H., and S.C.B.M. conceptualized the research. M.H. and S.C.B.M. supervised the research. P.D. performed the experiments, sample fabrication, AFM, electrical measurements and wrote the initial draft of the manuscript. M.H. performed the GIWAXS measurements and analysis. M.L. performed the wire SEM characterization and image analysis. K.H. performed the contact angle and surface energy measurements. T.L. transferred the wires on to the TEM grid by using the thermal transfer technique while D.P. performed the film/wire SAED/TEM characterization. All authors contributed to the preparation of the manuscript and approved the final version.

Data Availability Statement

The data that support the findings of this study are available from the corresponding author upon reasonable request.

Keywords

conjugated polymers, micro/nano wires, organic field effect transistors, solution shearing

Received: August 31, 2023
Published online:

[1] Y. Diao, L. Shaw, Z. Bao, S. C. B. Mannsfeld, *Energy Environ. Sci.* **2014**, *7*, 2145.
[2] C. Teixeira Da Rocha, G. Qu, X. Yang, R. Shivhare, M. Hambsch, Y. Diao, S. C. B. Mannsfeld, *ACS Appl. Mater. Interfaces* **2019**, *11*, 30079.
[3] M. Hambsch, T. Erdmann, A. R. Chew, S. Bernstorff, A. Salleo, A. Kiriy, B. Voit, S. C. B. Mannsfeld, *J. Mater. Chem. C* **2019**, *7*, 3665.
[4] J. Rivnay, S. C. B. Mannsfeld, C. E. Miller, A. Salleo, M. F. Toney, *Chem. Rev.* **2012**, *112*, 5488.
[5] G. Qu, J. J. Kwok, E. Mohammadi, F. Zhang, Y. Diao, *ACS Appl. Mater. Interfaces* **2018**, *10*, 40692.
[6] C. Farcau, H. Moreira, B. Viallet, J. Grisolia, L. Ressier, *ACS Nano* **2010**, *4*, 7275.
[7] Y. Diao, B. C.-K. Tee, G. Giri, J. Xu, D. H. Kim, H. A. Becerril, R. M. Stoltenberg, T. H. Lee, G. Xue, S. C. B. Mannsfeld, Z. Bao, *Nat. Mater.* **2013**, *12*, 665.
[8] V. Vohra, W. Mróz, S. Inaba, W. Porzio, U. Giovanella, F. Galeotti, *ACS Appl. Mater. Interfaces* **2017**, *9*, 25434.
[9] K. J. Park, C. W. Kim, M. J. Sung, J. Lee, Y. T. Chun, *Electron.* **2022**, *11*, 648.
[10] J. H. Kim, D. H. Lee, D. S. Yang, D. U. Heo, K. H. Kim, J. Shin, H.-J. Kim, K.-Y. Baek, K. Lee, H. Baik, M. J. Cho, D. H. Choi, *Adv. Mater.* **2013**, *25*, 4102.
[11] D. Wang, L. Lu, Z. Zhao, K. Zhao, X. Zhao, C. Pu, Y. Li, P. Xu, X. Chen, Y. Guo, L. Suo, J. Liang, Y. Cui, Y. Liu, *Nat. Commun.* **2022**, *13*, 6214.
[12] W. Liu, C. Wang, Q. Chen, J. Ding, G. Zhu, *ACS Appl. Electron. Mater.* **2023**, *5*, 1131.
[13] Y. Yabuuchi, Y. Minowa, H. Kajii, S. Nagano, A. Fujii, M. Ozaki, *Adv. Electron. Mater.* **2021**, *7*, 2100313.
[14] C. Luo, A. K. K. Kyaw, L. A. Perez, S. Patel, M. Wang, B. Grimm, G. C. Bazan, E. J. Kramer, A. J. Heeger, *Nano Lett.* **2014**, *14*, 2764.
[15] Y. Li, D. Ji, J. Liu, Y. Yao, X. Fu, W. Zhu, C. Xu, H. Dong, J. Li, W. Hu, *Sci. Rep.* **2015**, *5*, 13195.
[16] Y. Zhang, Y. Guo, L. Song, J. Qian, S. Jiang, Q. Wang, X. Wang, Y. Shi, X. Wang, Y. Li, *J. Mater. Chem. C* **2017**, *5*, 11246.
[17] L. Huang, Z. Wang, J. Chen, B. Wang, Y. Chen, W. Huang, L. Chi, T. J. Marks, A. Facchetti, *Adv. Mater.* **2021**, *33*, 2007041.
[18] Y. Lei, P. Deng, Q. Zhang, Z. Xiong, Q. Li, J. Mai, X. Lu, X. Zhu, B. S. Ong, *Adv. Funct. Mater.* **2018**, *28*, 1706372.
[19] J. Lenz, M. Statz, K. Watanabe, T. Taniguchi, F. Ortmann, R. T. Weitz, *J. Phys. Mater.* **2023**, *6*, 15001.
[20] H. A. Um, D. H. Lee, D. U. Heo, D. S. Yang, J. Shin, H. Baik, M. J. Cho, D. H. Choi, *ACS Nano* **2015**, *9*, 5264.
[21] J. Zessin, Z. Xu, N. Shin, M. Hambsch, S. C. B. Mannsfeld, *ACS Appl. Mater. Interfaces* **2019**, *11*, 2177.
[22] N. Shin, J. Zessin, M. H. Lee, M. Hambsch, S. C. B. Mannsfeld, *Adv. Funct. Mater.* **2018**, *28*, 1802265.
[23] N. Shin, K. S. Schellhammer, M. H. Lee, J. Zessin, M. Hambsch, A. Salleo, F. Ortmann, S. C. B. Mannsfeld, *Adv. Mater. Interfaces* **2021**, *8*, 2100320.
[24] Z. Zhang, X. Ren, B. Peng, Z. Wang, X. Wang, K. Pei, B. Shan, Q. Miao, P. K. L. Chan, *Adv. Funct. Mater.* **2015**, *25*, 6112.
[25] Y. Ito, A. A. Virkar, S. Mannsfeld, J. H. Oh, M. Toney, J. Locklin, Z. Bao, *J. Am. Chem. Soc.* **2009**, *131*, 9396.
[26] D. Janssen, R. De Palma, S. Verlaak, P. Heremans, W. Dehaen, *Thin Solid Films* **2006**, *515*, 1433.
[27] A. Armin, P. Wolfer, P. E. Shaw, M. Hambsch, F. Maasoumi, M. Ullah, E. Gann, C. R. Mcneill, J. Li, Z. Shi, P. L. Burn, P. Meredith, *J. Mater. Chem. C* **2015**, *3*, 10799.
[28] M. Li, C. An, T. Marszalek, M. Baumgarten, H. Yan, K. Müllen, W. Pisula, *Adv. Mater.* **2016**, *28*, 9430.
[29] C. Liu, W. Hu, H. Jiang, G. Liu, C. C. Han, H. Sirringhaus, F. Boué, D. Wang, *Macromolecules* **2020**, *53*, 8255.
[30] Y. Xi, C. M. Wolf, L. D. Pozzo, *Soft Matter* **2019**, *15*, 1799.
[31] Y. Minowa, Y. Yabuuchi, S. Nagano, S. Nagamatsu, A. Fujii, M. Ozaki, *ACS Appl. Mater. Interfaces* **2022**, *14*, 50112.
[32] J. A. Reinspach, Y. Diao, G. Giri, T. Sachse, K. England, Y. Zhou, C. Tassone, B. J. Worfolk, M. Presselt, M. F. Toney, S. Mannsfeld, Z. Bao, *ACS Appl. Mater. Interfaces* **2016**, *8*, 1742.
[33] K. Ditte, N. Kiriy, J. Perez, M. Hambsch, S. C. B. Mannsfeld, Y. Krupskaya, R. Maragani, B. Voit, F. Lissel, *Polymers* **2021**, *13*, 1435.
[34] K. Ditte, J. Perez, S. Chae, M. Hambsch, M. Al-Hussein, H. Komber, P. Formanek, S. C. B. Mannsfeld, A. Fery, A. Kiriy, F. Lissel, *Adv. Mater.* **2021**, *33*, 2005416.
[35] L. Yang, Y. Wu, Y. Yan, Z. Wang, Y. Qiao, D. Chang, C. Zhang, Y. Wang, X. Lu, Y. Liu, Y. Zhao, *Adv. Funct. Mater.* **2022**, *32*, 2202456.
[36] H. H. Choi, K. Cho, C. D. Frisbie, H. Sirringhaus, V. Podzorov, *Nat. Mater.* **2017**, *17*, 2.
[37] Y. Sato, S. Nakajima, N. Shiraga, H. Atsumi, S. Yoshida, T. Koller, G. Gerig, R. Kikinis, *Med. Image Anal.* **1998**, *2*, 143.
[38] C. Steger, *IEEE Trans. Pattern Anal. Mach. Intell.* **1998**, *20*, 113.
[39] T. Wagner, M. Hiner, xraynaud, *Thorstenwagner/Ij-Ridgedetection Ridge Detect. 1.4.0. Zenodo*. **2017**. https://doi.org/10.5281/zenodo.845874

